Research Article

Kinetic separation of CO_2/CH_4 mixtures with Ni-MOF-74@Al_2O_3 core–shell composites

D. Otter[1] · S.-J. Ernst[2] · L. Krätz[1] · H.-J. Bart[1]

Received: 21 January 2020 / Accepted: 7 May 2020 / Published online: 14 May 2020

Abstract
A novel core–shell species for the adsorption-based separation of carbon dioxide (CO_2) from methane (CH_4) is introduced by hydrothermal synthesis of Ni-MOF-74 on mesoporous spherical Al_2O_3 carrier substrate. The material was characterized and the shell thickness determined by means of optical and scanning electron microscopy as well as volumetric adsorption and fluid displacement experiments. Kinetic experiments with Ni-MOF-74@Al_2O_3 core–shell composites carried out at 303.15 K and at pressures up to 10 bar expose remarkably dominating uptake rates for CO_2 over CH_4. In the contrary Ni-MOF-74@Al_2O_3 appears to be unselective according to equilibrium data at the same conditions. Dynamic breakthrough experiments of binary CH_4/CO_2-mixtures (at 303.15 K and 5 bar) prove the prevailing effect of adsorption kinetics and the storage function of the mesoporous core. This statement is supported by a considerable boost in CO_2-selectivity and capacity compared to adsorption equilibria measured on pure Ni-MOF-74 by the factor of 55.02 and up to 2.42, respectively.

Keywords Kinetic separation · Core–shell · Composite materials · Dynamic adsorption · CO_2-separation · Separation efficiency improvement

List of symbols

a	Specific surface (–)
c	Concentration (mol m^{-3})
d	Diameter (m)
g	Gibbs free energy (J mol^{-1})
k_{eq}	Equilibrium constant (bar^{-n})
L	Length (m)
n	Number of moles/inverse superscript (Sips) (mol)
p	Pressure (Pa)
r	Radius (m)
R	Universal gas constant (J mol^{-1} K^{-1})
t	Thickness (m)
T	Temperature (K)
$\dot{V}$	Flow rate (m^3 s^{-1})
v_p	Pore volume (m^3)
w	Mass fraction (–)
X	Loading (adsorbed phase) (mol g^{-1})
x	Mole fraction (adsorbed phase) (–)
$\bar{x}$	Adsorbed phase composition vector (–)
y	Mole fraction (gas phase) (–)
z	Reduced spreading pressure (J m^{-3})

Greek symbols

α	Separation factor (–)
γ	Activity coefficient (–)
ε	Void fraction (–)
Π	Spreading pressure (J m^{-3})
ρ_m	Material density (kg m^{-3})
ρ_p	Particle density (kg m^{-3})
φ	Volume fraction (–)

Subscripts

bed	Bed
c	Core
cs	Core–shell

✉ H.-J. Bart, bart@mv.uni-kl.de | [1]Lehrstuhl für Thermische Verfahrenstechnik, Technische Universität Kaiserslautern, Gottlieb-Daimler-Straße 44, 67663 Kaiserslautern, Germany. [2]Institut für Solare Energiesysteme (ISE), Fraunhofer-Gesellschaft, Heidenhofstraße 2, 79110 Freiburg im Breisgau, Germany.

h	Hybrid
max	Maximum
s	Shell
t	Total
i	Component i

1 Introduction

The separation of gas mixtures is a common unit operation in chemical process industry. In general, organic and inorganic gases and vapors are widely used, e.g. as educts for chemical processes, as energy carriers or industrial gases. There is a certain demand for natural gas [1] or lower hydrocarbons for either heating purposes or fuel cell drives [2]. Additionally, in biogas fermentation a low-calorific gas mixture with the main components methane (CH_4), carbon dioxide (CO_2) and water vapor (H_2O) as well as small amounts of other components such as hydrogen sulphide (H_2S) and ammonia (NH_3) is produced. The separation of water vapor (H_2O) and H_2S avoids the formation of corrosive acids whereas the separation of CO_2 increases the net calorific value to an extent that meets the requirements for biomethane quality, which is mandatory for the injection into the natural gas grid [3]. Large scale CO_2 scrubbing processes are commonly based on reactive chemical solvents, which are subject to high thermal and chemical stress during the regeneration cycles. This can reduce the solvents service life due to degradation and finally results in high demands for resources and energy [4, 5].

Adsorption processes offer an ecological and economical alternative to solvent-based gas scrubbing. Metal–organic framework compounds (MOFs) are a new class of highly porous coordination networks with high specific surfaces and pore volumes. Their modular structure consists of metal ions or metal containing clusters which are connected to each other by organic molecules known as linkers. By selecting the individual structural elements, characteristic properties such as the pore size and geometry as well as chemical functionality of the pore walls can be precisely adjusted to the desired task in gas separation and storage [6]. Long-term stability in humid, acidic or solvent-containing atmospheres is important for practical use.

During synthesis MOFs usually accumulate as fine powders, which are naturally difficult to handle in large scale adsorption plants. In order to improve the process technology, the powdery MOFs are synthesized directly as larger particles while retaining their characteristic properties such as specific surface and porosity [7]. However, the growing of large crystals [8] or the synthesis of MOF pellets [9] requires large amounts of expensive raw materials. Therefore, hierarchically structured, MOF-based functional materials, better known as core–shell composites, are attracting increasing attention. These consist of a porous core carrier material (e.g. oxide ceramics), with a thin selective MOF layer coated on its surface. The motivation is to utilize the void volume of an unselective and easily available, mesoporous core material as extra storage for the target component by coating it with a thin and highly selective MOF layer.

The combined effect of the individual composite functionalities also produces new and more valuable properties, often superior to its constituents [10, 11]. A theoretical study on CO_2 separation from CO_2/CH_4 mixtures has shown that spherical core–shell adsorbents made from inert 2860 µm diameter mullite cores and covered with 70 µm thin CO_2-selective SAPO-34 shells are more efficient than pure SAPO-34 adsorbents [12]. Compared to the porous adsorbent made of pure MOF material, the core–shell morphology requires considerably less MOF substance.

Core–shell composites were also found to be suitable as stationary phase in gas chromatographic analysis. Investigations on spherical microporous/mesoporous NH_2-MIL-53(Al)@SiO_2 core–shell composites have shown that the MOF shell controls the access of guest molecules (N_2) to the hydrophilic mesoporous SiO_2 structure [13]. Also in hierarchical microporous/mesoporous ZIF-8@SiO_2 composites, the ZIF-8 shell, consisting of a network of micropores and accessible via ultra-microporous windows of 3.4 Å, is determining the passage of the guest molecules to the mesoporous silica nucleus [14].

Core–shell composites are also suitable for decomposing gas mixtures (e.g. flue gas, [15]). The MOF shell, which is in contact with the flue gas, has the task of selecting carbon dioxide, which diffuses further into the mesoporous core. The latter acts as a gas storage that can be regenerated under mild conditions. The use in moist and acid atmospheres caused by the simultaneous occurrence of CO_2 and water vapor requires stable MOFs. A suitable species with high hydrothermal stability is the nickel dihydroxy terephthalate Ni-MOF-74 [15] used in this study for the separation of CH_4/CO_2 mixtures.

2 Materials and methods

2.1 Material synthesis

The production of pure Ni-MOF-74 was executed by a hydrothermal synthesis according to Dasgupta and Dietzel [15, 16]. At first two aqueous precursor solutions were prepared by separately dissolving nickel(II) acetate tetrahydrate (> 99% from Sigma-Aldrich) and

2,5-dihydroxyterephthalic acid (98% from Sigma-Aldrich) in water. The exact compositions were 7.466 g $Ni(CH_3COO)_2$ x 4 H_2O and 2.072 g $(HO)_2C_6H_2$-1,4-$(CO_2H)_2$ each in 50 mL deionized water, resulting in solutions with molarities of 0.6 mol L^{-1} and 0.21 mol L^{-1}, respectively. Both solutions are poured together in an autoclave and sealed at ambient conditions. Subsequently the autoclave is tempered to 120 °C for 70 h. The obtained crystals are mechanically separated from the liquid, purged with ethanol and deionized water and finally activated inside a vacuum furnace at 140 °C. The production of the core–shell composites was carried out by following the equal route of synthesis whereas mesoporous Al_2O_3 spheres with an average diameter of 3.2 mm were used as crystallization nuclei (see Fig. 1).

2.2 Material characterization

Figure 2 illustrates, the XRD patterns of both, the pure Ni-MOF-74 and the Ni-MOF-74@Al_2O_3 core–shell composite, hereinafter also referred as hybrid material, which are revealing their peaks at the same rotation angles. This indicates that a pure layer of Ni-MOF-74 is deposited on the outer surface of the spherical Al_2O_3 carrier

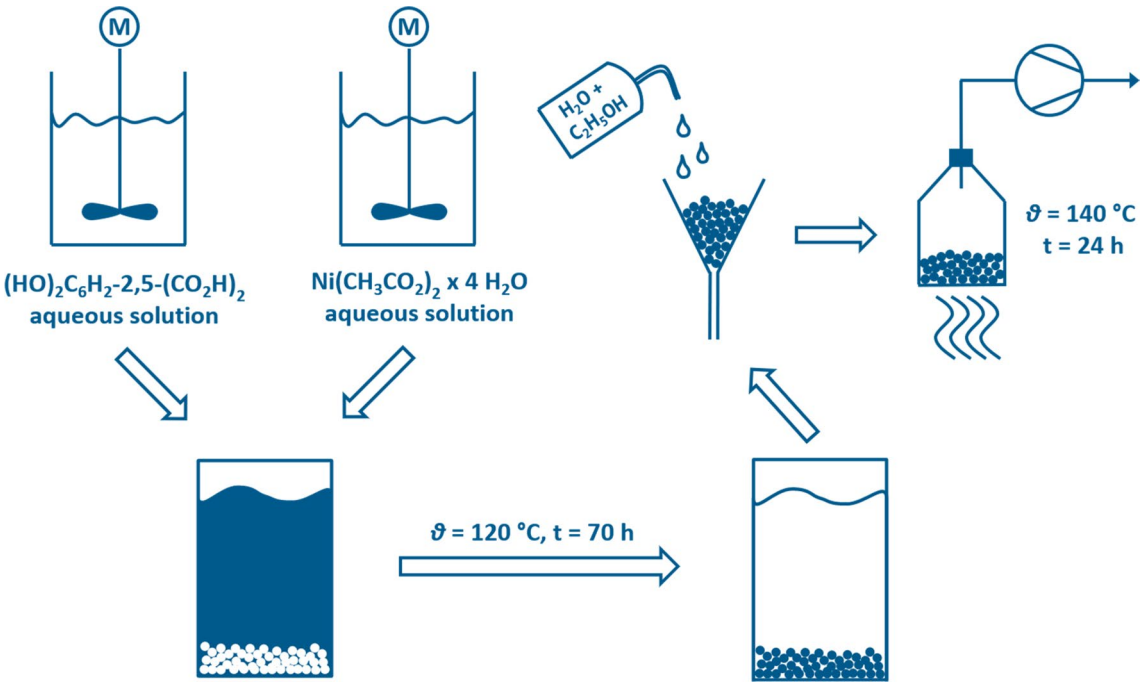

Fig. 1 Schematic for the synthesis of Ni-MOF-74@Al_2O_3 core–shell composites

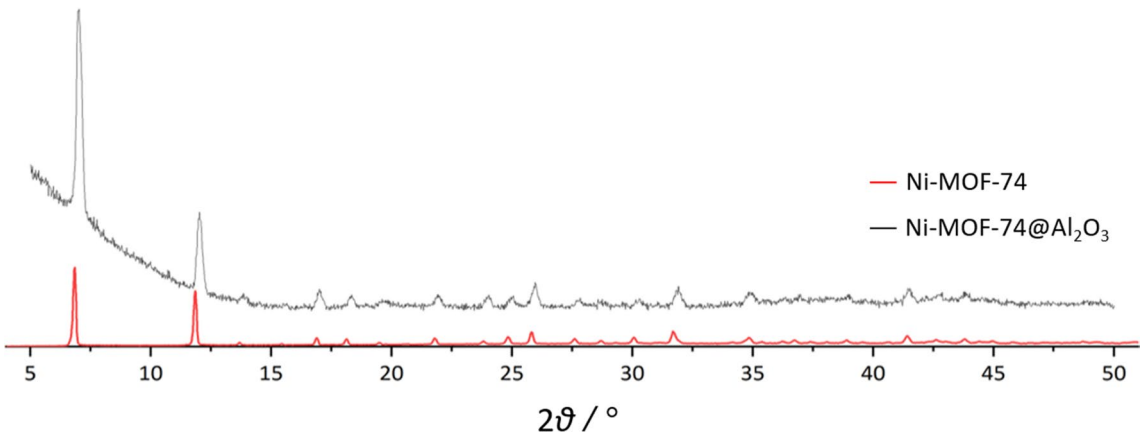

Fig. 2 XRD pattern of Ni-MOF-74 (red) and the Ni-MOF-74@Al_2O_3 core–shell composite (black)

matrix without any mayor inclusion of impurities. This observation coincides with images of the particle cross section generated by means of light scanning microscopy (Olympus LEXT). For this reason the sample was prepared by pouring the hybrid particles into a matrix of epoxy resin and grounding them down to the hemisphere. Figure 3a, b prove that the Al_2O_3 core is fully coated with a continuous layer of Ni-MOF-74.

According to the SEM images of the inner cross section of a bisected core–shell sphere taken with FEI Helios Nanolab 650, depicted in Fig. 4, it can be distinguished between the mesoporous Al_2O_3 core with its rough crystal morphology and the more uniformly and dense

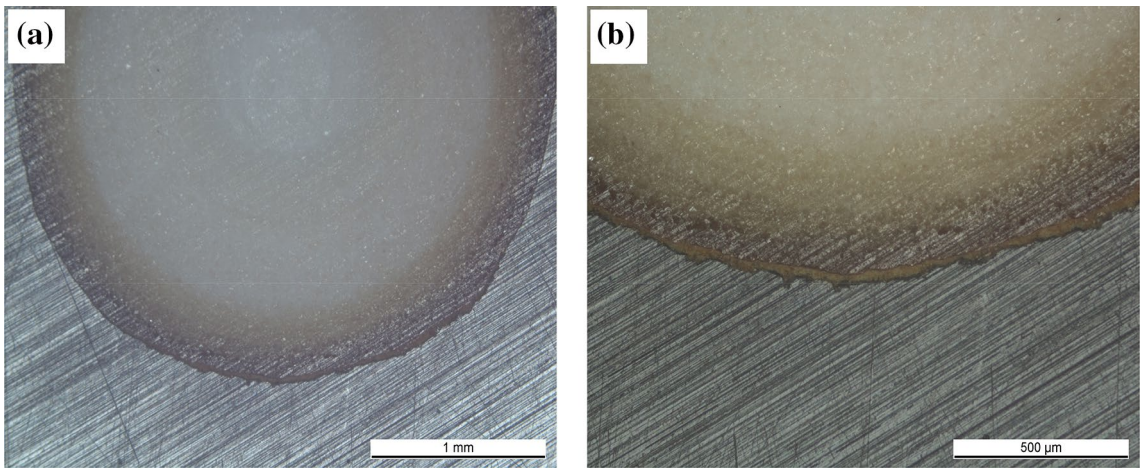

Fig. 3 Optical microscope image of the layer surface (**a**) and the layer cross section (**b**) of a Ni-MOF-74@Al_2O_3 core–shell sphere

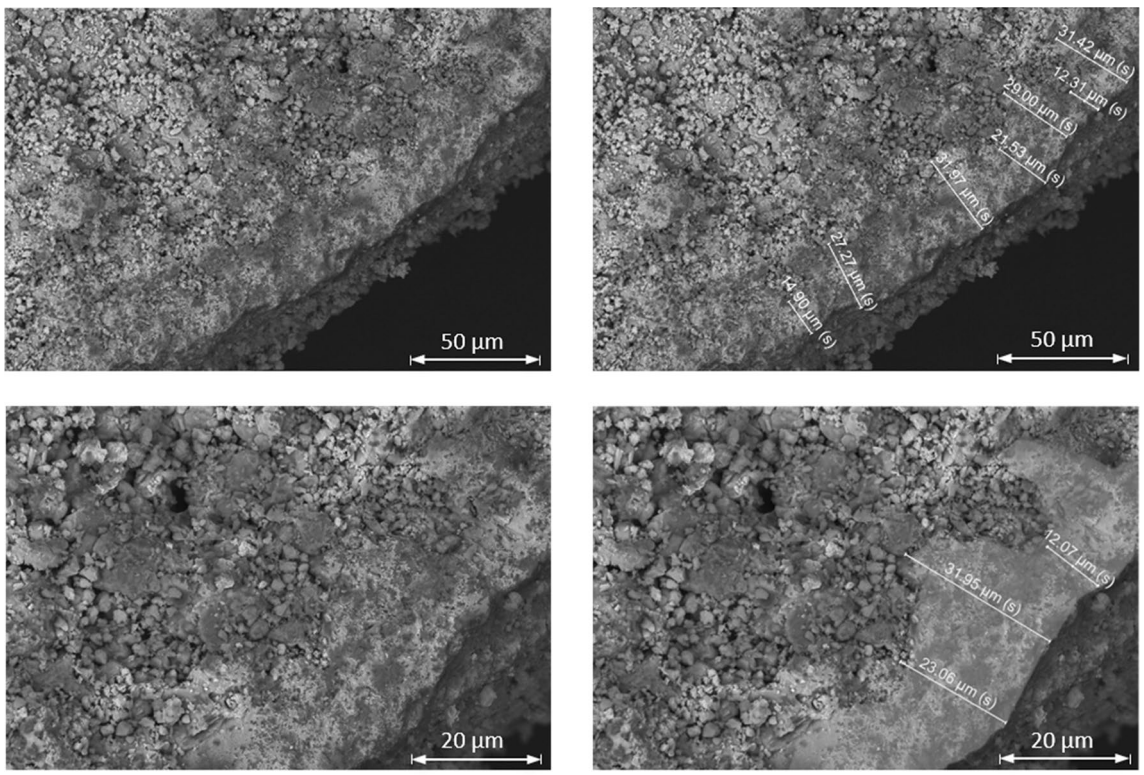

Fig. 4 SEM raw images of the cross section of a bisected Ni-MOF-74@Al_2O_3 core–shell sphere with a magnification factor of 1000 (**a**) and 2000 (**b**) with additional auxiliary lines color accentuation for highlighting the Ni-MOF-74 shell (*)

microporous Ni-MOF-74 layer. The thickness of the latter is very inhomogeneous and varies from approximately 1 µm up to 40 µm with an assumed average of 5–10 µm. For the purpose of better visualization an excerpt with comparatively large shell thickness was chosen.

For further material characterization of the specific surface, the pore volume and the material density of the pure materials, Ni-MOF-74 and Al_2O_3, as well as the core–shell composite was determined by means of volumetric adsorption (NOVA 2000e, Quantachrome) and fluid displacement experiments (Ultrapyc 1000 T, Quantachrome), respectively (see Table 1). The specific surface was calculated by applying the standard BET method for adsorption isotherms measured at 77.15 K using nitrogen (N_2) as adsorptive. As expected, the value determined for the specific surface area of the core–shell is found between the values of the pure components. The determination of the pore size distribution and pore volume was carried out using the adsorptive N_2 at 77.15 K for the mesoporous Al_2O_3 and the adsorptive CO_2 at 273.15 K for the microporous Ni-MOF-74, by applying the non-linear density functional theory (NLDFT).

For the analytical evaluation of the adsorption experiments (see Sect. 2.3) the determination of the shell thickness is of high importance. The shell thickness was mathematically estimated from experimental data (see Table 1) by postulating two different geometric approaches for the hybrid material based on the microscope images (see Fig. 5). A simple geometric model (see Fig. 5a), which is in agreement to the SEM-images (see Fig. 4), considers the core–shell particle as two totally separate and independent compartments, the inner core of pure Al_2O_3 and the distinct shell of pure Ni-MOF-74. However, taking a look at Fig. 3b advises the assumption of a hybrid layer being formed within the outer region of the Al_2O_3 core due to crystallization of Ni-MOF-74 inside the mesopores of the latter. The second model takes these assumptions into account (see Fig. 5b) by dividing the core–shell particle in three compartments. The first compartment is the Al_2O_3 core, the second compartment is the Ni-MOF-74/Al_2O_3 hybrid layer within the core and the third compartment consist of a pure Ni-MOF-74 shell. The following calculations are based on the assumption of the core–shell composites being ideal monospheres with a diameter of 3.2 mm.

Table 1 Specific surface (a), pore volume (v_p), material density (ρ_m), void fraction (ε) and particle density (ρ_p) of Ni-MOF-74, Al_2O_3 and Ni-MOF-74@Al_2O_3 core–shell composites

Adsorbent	a ($m^2\ g^{-1}$)	v_p (cm^3 g)	ρ_m (g cm^{-3})	ε (–)	ρ_p (g cm^{-3})
Ni-MOF-74	1293[a]	0.49[b]	2.11[d]	0.51	1.04
Al_2O_3	264[a]	0.35[c]	2.94[d]	0.51	1.44
Core–shell	295[a]	0.30[c]	2.71[d]	0.45	1.50

[a]Derived from adsorption isotherm with N_2 at 77.15 K by applying the BET-method

[b]Derived from adsorption isotherm with CO_2 at 273.15 K by applying NLDFT

[c]Derived from adsorption isotherm with N_2 at 77 K by applying NLDFT

[d]Derived from volumetric fluid displacement experiment with He at STP applying Boyle's law

For the first approach, based on the simple geometric model, the hypothetical shell thickness was determined by linear interpolation of the pure components' specific surfaces (Eq. 1) introducing their mass fractions as weighting factors (Eqs. 2, 3):

$$a_{cs} = w_c a_c + w_s a_s \tag{1}$$

with

$$w_c = \frac{r_c^3 \rho_{p,c}}{r_c^3 \rho_{p,c} + \left[\left(r_c + t_s\right)^3 - r^3\right]\rho_{p,s}} \tag{2}$$

$$w_s = 1 - w_c \tag{3}$$

where a_{cs}, a_c and a_s denote the specific surfaces of the entire core–shell composite, the core and the shell, respectively. The same holds for the mass fraction w and the particle density ρ_p. This results in a mass fraction of Ni-MOF-74 of 3.0 percent and a hypothetical average shell

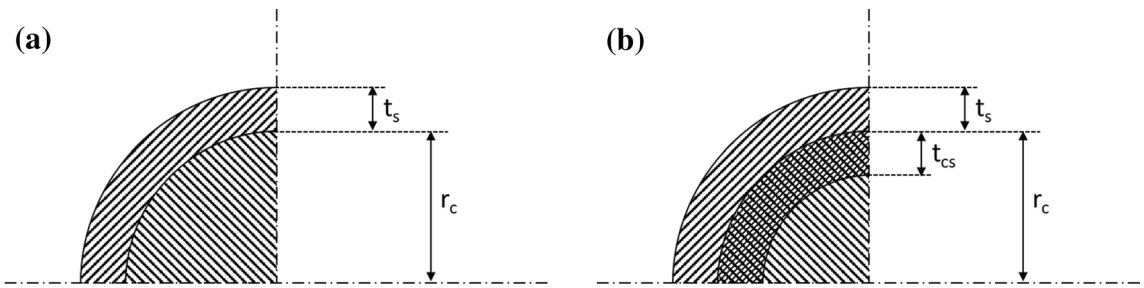

Fig. 5 Scheme of the geometric model used for the calculation of the shell thickness from specific surface data (**a**) and from density data (**b**)

thickness of 45 µm, which is in good agreement to the SEM images (see Fig. 5) with a slight overestimation of the shell thickness.

By applying the second and more complex geometric model an approach for the core–shells particle density can be derived based on the particle densities of the pure components by means of extrapolation (see Eq. 4). This procedure allows the iterative calculation of the volume fractions which have to be assigned for the second and third compartment and their shell-thickness, respectively [see Eqs. (5)–(7)]

$$\rho_{p,cs} = \varphi_c \rho_{p,c} + \varphi_h \rho_{p,h} + \varphi_s \rho_{p,s} \tag{4}$$

where

$$\varphi_c = \frac{\left(r_c - t_h\right)^3}{\left(r_c + t_s\right)^3} \tag{5}$$

$$\varphi_h = \frac{r_c^3 - \left(r_c - t_h\right)^3}{\left(r_c + t_s\right)^3} \tag{6}$$

$$\varphi_s = \frac{\left(r_c + t_s\right)^3 - r_c^3}{\left(r_c + t_s\right)^3} \tag{7}$$

The particle density represents a function of the pore volume and the material density [see Eqs. (8)–(10)].

$$\rho_{p,c} = \left(1 - \varepsilon_c\right)\rho_{m,c} \tag{8}$$

$$\rho_{p,s} = \left(1 - \varepsilon_s\right)\rho_{m,s} \tag{9}$$

$$\rho_{p,h} = \left(1 - \varepsilon_c\right)\rho_{m,c} + \varepsilon_c \rho_{p,s} \tag{10}$$

The assignment of the formula symbols remains the same as in the previous contemplation where φ denotes the volume fraction. The newly introduced hybrid layer is considered by the index *h*.

Solving the equation system for given $\rho_{p,cs}$ yields a thickness of 5 µm for the outer pure Ni-MOF-74 shell (third compartment) and 128 µm for the inner hybrid shell (second compartment) summing up in an overall mass fraction of 0.046 of pure Ni-MOF-74 within the core–shell composite. This solution shows very high agreement with the information gained from the microscope images. However, this solution tends to overestimate the reality because some of the mesopores of the Al_2O_3 core can most likely not be penetrated by gas molecules anymore since they are being blocked due to synthesis. This results in an underestimation of the total pore volume with regards to the fluid displacement experiments. The same holds for the pore surface but with slighter impact onto the result as the volume to surface ratio is relatively high for mesopores compared to micropores. It can be assumed that the actual shell thickness meets a compromise between both solutions. Subsequently the mass fraction of Ni-MOF-74 within the core–shell-composite can be estimated to values between 3 and 4.6%.

2.3 Experimental setup

2.3.1 Equilibrium apparatus

A gravimetric equilibrium apparatus (IGA-002, Hiden Isochema) was used to determine the time dependent sample uptake (adsorption dynamics) and the isotherms (adsorption equilibria) for pure adsorptivs. The integrated precision balance with a resolution of 10^{-7} g enables to record the adsorbent load for each pressure level approached until the thermodynamic equilibrium is reached, and thus allows conclusions to be drawn about the adsorption kinetics. As a termination criterion, it was assumed that the equilibrium condition is fulfilled as soon as the weight gain due to the adsorption is less than 10^{-7} g per min for a period of 15 min. The system can be pressurized up to 10 bar. The sample is heated in situ by an electric heating element, while the temperature is controlled when the test is carried out using a high-performance circulation thermostat with integrated Peltier technology (Lauda, Loop L 250). As adsorptives only pure gases (Air Liquide, $y_i > 99.999\%$) were used.

2.3.2 Packed bed adsorber (breakthrough plant)

The experimental setup for the determination of breakthrough curves of gas mixtures can be divided into three subsystems (see Fig. 6). Gas dosing system (I), adsorber (II), gas analysis (III).

Using the gas dosing system (I), consisting of three thermal mass flow controllers (MFC 1–3), ternary gas mixtures of any composition can be generated, which can optionally be moistened by forced flow through a bubbler system (B 1). The gas mixture generated in the dosing station can either be sent through the adsorber unit (II) or directly to the gas analysis (III) via bypass. The adsorber unit consists of an autoclave (A 1, $d_{bed} = 1.5$ cm, $L_{bed} = 15$ cm), which is installed in a GC oven (O 1, T = 30–300 °C) and therefore allows the in situ activation and regeneration of the sample. According to Kwapinski et al. [17] the column to particle ratio should exceed the value of 10, however, the sample amount and available equipment could not satisfy this requirement. Nevertheless, reliable and reproducible data could be generated from break through experiments

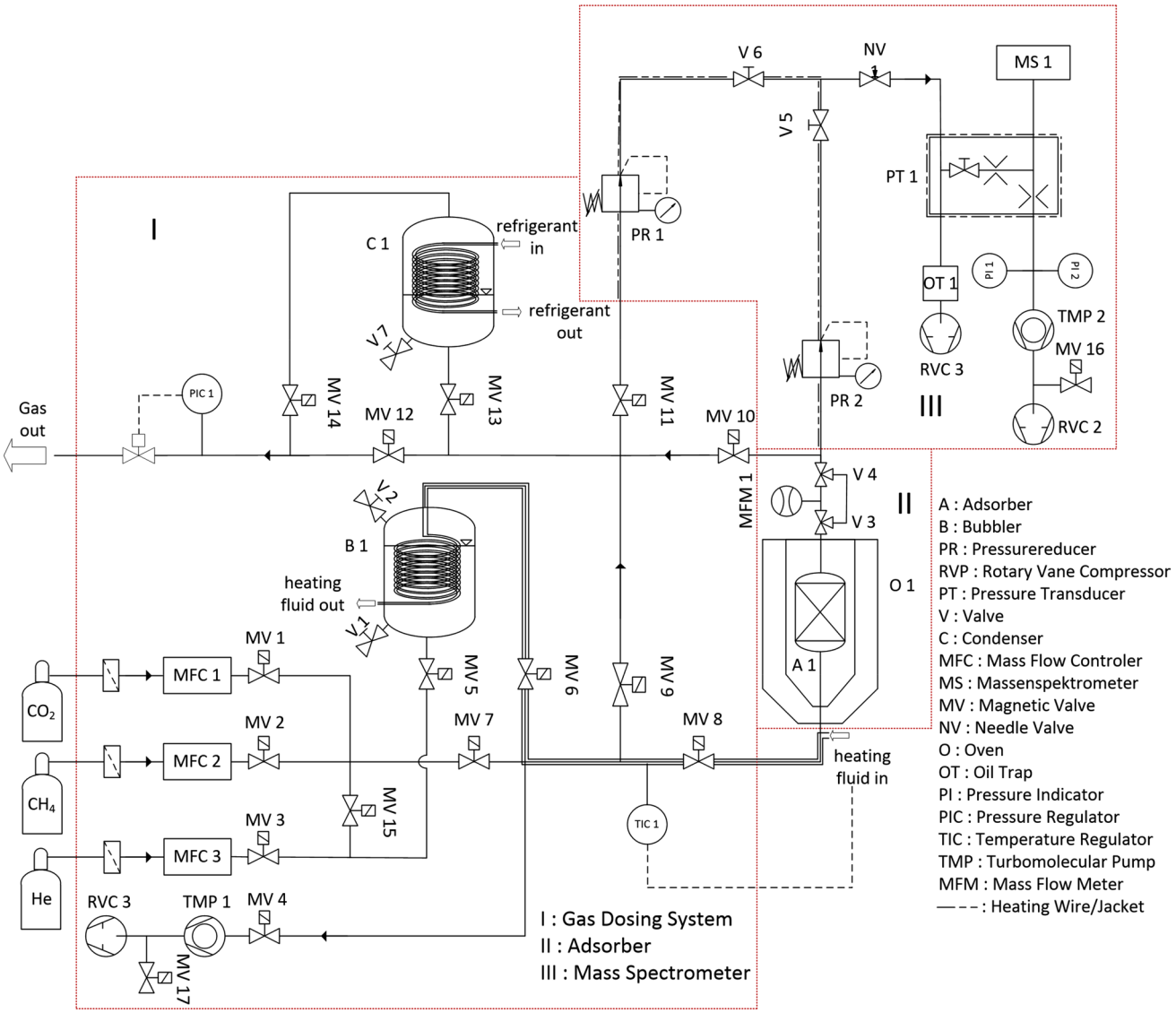

Fig. 6 Flow chart of the breakthrough plant including gas dosing system (I), adsorber (II), gas analysis (III)

(see Sect. 3.2). In order to record the change in volume flow due to adsorption, a thermal mass flow meter is installed downstream of the adsorber. A quadrupole mass spectrometer records the composition of the gas mixture both in front of the adsorber—via bypass—and behind the adsorber in high time resolution and precision.

3 Adsorption analysis

3.1 Adsorption dynamics and equilibria

For further material characterization adsorption equilibria and dynamics were investigated with a gravimetric apparatus (see Sect. 2.3.1). Figure 7 illustrates the adsorption isotherms of CH_4 and CO_2 on Ni-MOF-74 at a temperature of 30 °C. Adsorptive CO_2 at Ni-MOF-74 shows a type I isotherm behavior and can be most accurately described with the Sips model (see Eq. (11), [18, 19]),

$$X_i = X_{i,max} \frac{k_{i,eq} p_i^{1/n_i}}{1 + k_{i,eq} p_i^{1/n_i}} \tag{11}$$

whereas for CH_4 the equilibrium uptake appears to increase almost linearly with the pressure—at least for pressures below 10 bar—also exhibiting the Sips equation as the most suitable model. According to equilibrium data Ni-MOF-74 seems to clearly favor CO_2 at lower pressure.

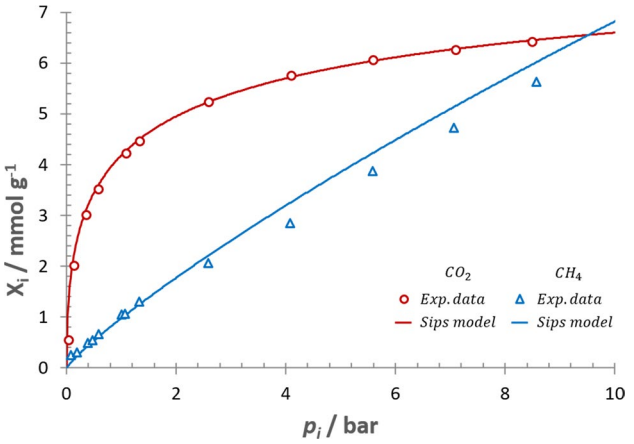

Fig. 7 Adsorption equilibria of Ni-MOF-74@Al_2O_3 with CO_2 (red) and CH_4 (blue) at $T = 303.15$ K approximated by the Sips isotherm

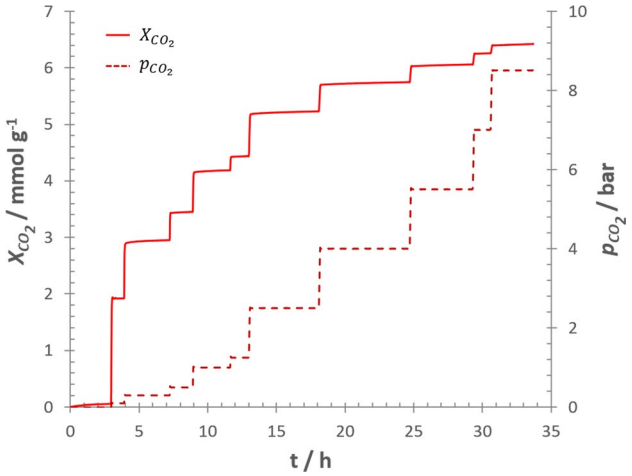

Fig. 8 Time dependent adsorption uptake response induced by a pressure profile of CO_2 imposed onto Ni-MOF-74 at $T = 303.15$

At higher pressure, however, the affinity switches to CH_4 which is indicated by the isotherms crossing when exceeding pressures over 9 bar.

Having a look at the dynamics of adsorption for Ni-MOF-74 reveals that CO_2 (see Fig. 8) reaches equilibrium almost instantly, whereas the uptake response for CH_4 appears to be very sluggish (see Fig. 9). Consequently, the adsorption kinetics for CO_2 must exceed those for CH_4 by several orders of magnitude. This gives rise to the assumption that Ni-MOF-74 is kinetically highly selective towards the key component CO_2. Thus, a selective layer of Ni-MOF-74 deposited on the surface of a rather unselective material like Al_2O_3 might result in an efficiency boost due to the available extra volume introduced by the employed core.

Figure 10 shows the adsorption equilibria of CO_2 and CH_4 on the hybrid material. According to the equilibrium uptake the hybrid material appears to favor CO_2 over CH_4 at pressures below 3.5 bar. At pressures beyond 3.5 bar, however, the equilibrium uptakes for CH_4 are higher than for CO_2. Nevertheless, the adsorption dynamics are exhibiting the same behavior as pure Ni-MOF-74 with a clear preference for CO_2 (see Figs. 11, 12).

Even though the equilibrium selectivity of the core–shell composite towards CO_2 is very low, the high kinetic selectivity towards the latter could overcompensate this drawback in terms of separation efficiency in a dynamic adsorption process.

3.2 Breakthrough experiments

As already discussed above, the most reliable information with regards to separation efficiency can be derived from dynamic breakthrough experiments. Figure 13 shows the concentration profile of methane and carbon dioxide at the outlet of a fixed bed (L = 15 cm, d = 1.5 cm, $m_{cs} = 15.7$ g) of Ni-MOF-74@Al_2O_3 at a constant binary feed flow of 50 mL min^{-1} (STP) with a molar fraction of 0.25 carbon dioxide at 30 °C and 5 bar.

As can be seen qualitatively the Ni-MOF-74@Al_2O_3 core–shell composite exhibits a good separation efficiency indicated by the distinct roll up of CH_4 and the delayed breakthrough of CO_2, respectively. Integration of breakthrough curves (BTC) yields the adsorption uptake by solving the global mass balance in Eq. (12), which can be simplified to Eq. (13) by assuming an ideal behavior of the gas phase, which is valid for low pressures and elevated temperatures.

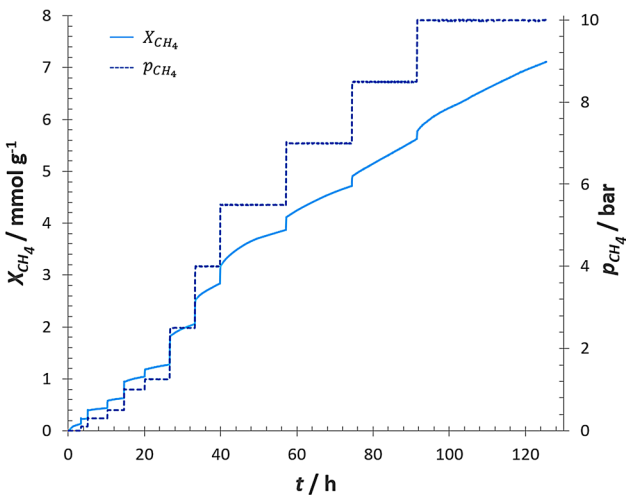

Fig. 9 Time dependent adsorption uptake response induced by a pressure profile of CH_4 imposed onto Ni-MOF-74 at $T = 303.15$ K

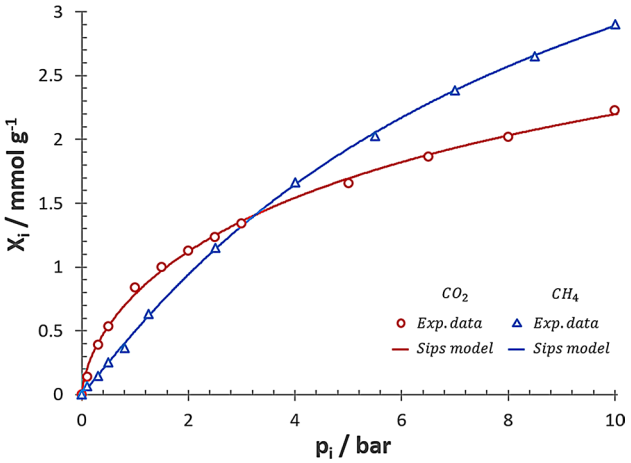

Fig. 10 Adsorption equilibria of Ni-MOF-74@Al_2O_3 with CO_2 (red) and CH_4 (blue) at $T = 303.15$ K approximated by the Sips isotherm

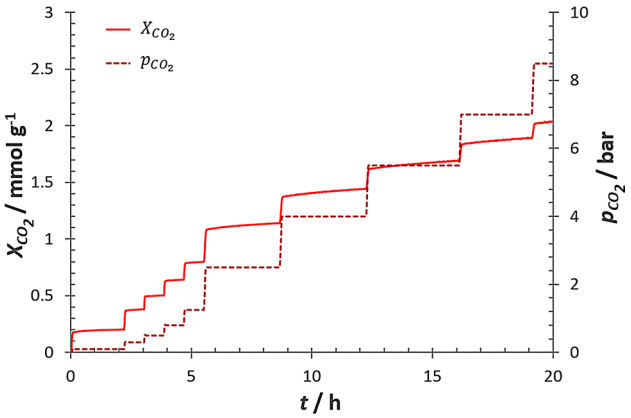

Fig. 11 Time dependent adsorption uptake response induced by a pressure profile of CO_2 imposed onto a sample of Ni-MOF-74@Al_2O_3 core–shell at $T = 303.15$ K

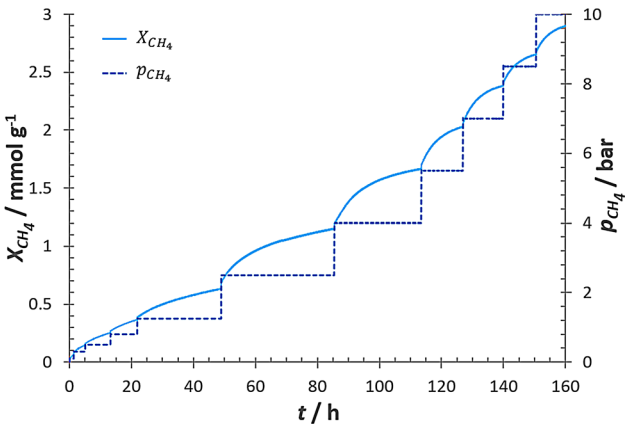

Fig. 12 Time dependent adsorption uptake response induced by a pressure profile of CH_4 imposed onto a sample of Ni-MOF-74@Al_2O_3 core–shell at $T = 303.15$ K

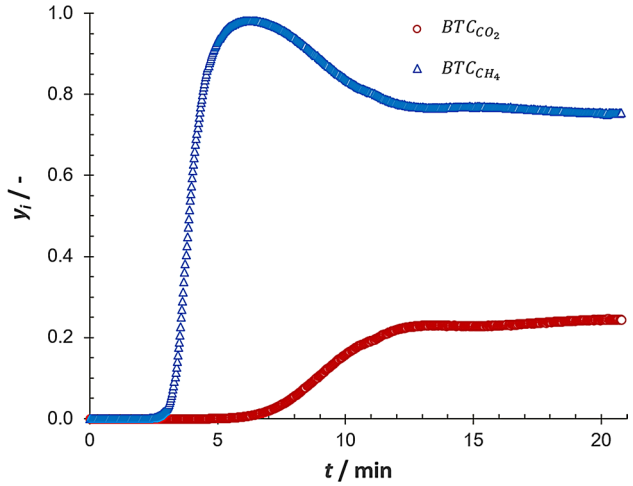

Fig. 13 Breakthrough curve (BTC) of a binary CH_4/CO_2-mixture ($y_{CO_2} = 0.25$) at $T = 303.15$ K, $p = 5$ bar and a flow rate of 50 mL min^{-1} (STP) on a fixed bed ($L_{bed} = 15$ cm, $d_{bed} = 1.5$ cm) of Ni-MOF-74@Al_2O_3 core–shell particles

$$n_{i,T,p}^{ads} = \int_{t_0}^{t_\infty} \left[\dot{V}_{in}(t)c_{i,in}(t) - \dot{V}_{out}(t)c_{i,out}(t)\right]dt \tag{12}$$

$$= \frac{p}{RT}\int_{t_0}^{t_\infty} \left[\dot{V}_{in}(t)y_{i,in}(t) - \dot{V}_{out}(t)y_{i,out}(t)\right]dt \tag{13}$$

The difference of the molar flow into and out of the fixed bed can be attributed to the adsorption sink. The molar flow out of the fixed bed can be simply derived by integrating the concentration profile and the volumetric flow rate over the time at the outlet of the adsorber. Whereas in order to estimate the quasi molar flow into the fixed bed the dead volume of the adsorber including the packed bed and its peripherical pipe system to the analytical device has to be considered. For this purpose, the residence time distribution (RTD, see Eq. (13)) was determined by carrying out the same experiment with the same experimental settings while the adsorbent was merely substituted with nonporous silica spheres of the same diameter. The integration of the detected concentration signal was conducted numerically by applying the trapezoidal rule (Eq. (14), [20]) on Eq. (13) yielding Eq. (15).

$$\int_{j=1}^{n-1} f(x)dx \approx \sum_{j=1}^{n-1} \left(x_{j+1} - x_j\right)\left(\frac{f\left(x_j\right) + f\left(x_{j+1}\right)}{2}\right) \tag{14}$$

$$n_{i,T,p}^{ads} = \frac{p}{2RT}\sum_{t_j=t_0}^{t_\infty-1}\{[\dot{V}_{in}(t_j)+\dot{V}_{in}(t_{j+1})]\,[\dot{y}_{i,in}(t_j)+\dot{y}_{i,in}(t_{j+1})] - [\dot{V}_{out}(t_j)+\dot{V}_{out}(t_{j+1})]\,[\dot{y}_{i,out}(t_j)+\dot{y}_{i,out}(t_{j+1})]\}(t_{j+1}-t_j) \quad (15)$$

The adsorbed amount as mathematically described in Eqs. (13) and (15), respectively, can be illustrated by the area which is enclosed between the RTD and the BTC of the individual species as shown in Fig. 14. For CO_2 the adsorbed amount adds up to 4.93 mmol. In contrast to this the integral analysis yields a CH_4 uptake of 0.02 mmol. This means the areas beneath (A_2) and beyond (A_3) the RTD are cancelling each other, which is also graphically indicated by the BTC crossing over the RTD after 4 min due to its roll up according to the enrichment of CH_4 at the adsorber outlet. Referred to the entire sample load of 15.7 g the average loading aggregates for CO_2 to 0.32 mmol and for CH_4 to 0.001 mmol per gram core–shell utilized. However, referred to the material of interest (Ni-MOF-74), whose mass fraction is estimated to be 3–4.6% (see Sect. 2), the calculated sample load increases for CO_2 to values between 6.85 and 10.51, for CH_4 to values between 0.03 and 0.05 mmol per gram Ni-MOF-74 utilized.

3.3 Evaluation of the results

For a convenient evaluation of the results a comparison of Ni-MOF-74@Al_2O_3 core–shell composites and pure Ni-MOF-74 has to be done by solely contemplating the species of interest, the selective Ni-MOF-74. This means, a comparison of adjusted adsorption data gained from the dynamic breakthrough experiments with hybrid material, which are referring just to the utilized Ni-MOF-74, to the equilibrium data measured on pure Ni-MOF-74 at the same conditions. The dynamic breakthrough experiments were carried out at 5 bar and 30 °C with a feed composition of 25 percent CO_2 and 75 percent CH_4, which are set to be the reference conditions. According to Daltons law the partial pressures of CO_2 and CH_4 sum up to 1.25 bar and 3.75 bar, respectively. Referring to the adsorption equilibria of Ni-MOF-74 at 30 °C (see Fig. 7) the uptake of pure CO_2 at 1.25 bar equals 4.41 mmol per g.

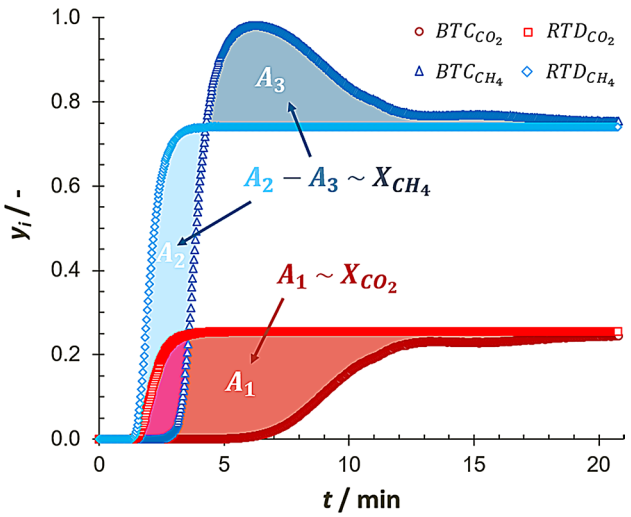

Fig. 14 Breakthrough curve (BTC) for Ni-MOF-74@Al_2O_3 and residence time distribution (RTD) for inert silica spheres of a binary CH_4/CO_2 mixture ($y_{CO_2}=0.25$) at $T=303.15$ K, $p=5$ bar and a flow rate of 50 mL min^{-1} (STP) on a fixed bed ($L_{bed}=15$ cm, $d_{bed}=1.5$ cm)

Under consideration of mixed gas adsorption another approach can be made by calculating the binary adsorption equilibrium from the single component equilibrium data using the ideal adsorbed solution theory (IAST, [21, 22]). The variation in the molar Gibbs free energy g at constant temperature T and spreading pressure Π is given by:

$$g(T,\Pi,\bar{x}) = RT\sum_{i=1}^{n} x_i \ln x_i\gamma_i(\Pi,T,\bar{x}) \quad (16)$$

where γ_i denotes the activity coefficient, x_i is the mole fraction of component i in the adsorbed phase and $\bar{x}$ the corresponding adsorbed phase composition vector. The relation of the fugacity of the gas phase and the adsorbed phase at thermodynamic equilibrium is described in analogy to Raoult's law for vapor liquid equilibria:

$$py_i = p_i^0(\Pi)x_i\gamma_i(\Pi,T,\bar{x}) \quad (17)$$

with the system pressure p and the mole fraction of component i in the gas phase y_i. The hypothetical equilibrium pressure p_i^0 of the pure component at the same spreading pressure and temperature of the given mixture can be obtained from:

$$z = \frac{\Pi a}{RT} = \int_{p_i=0}^{p_i^0}\frac{n_i(p_i)}{p_i}dp_i \quad (18)$$

Here z denotes the reduced surface potential, a the specific surface area of the adsorbent and $n_i(p_i)$ the adsorbed amount represented by the adsorption isotherm equation for the pure component i.

In order to determine the total amount adsorbed, n_t, in a multi component system the thermodynamic consistency given by the Gibbs–Duhem relation (Eq. 19, [23]) as well as the constraints for a closed system must be satisfied:

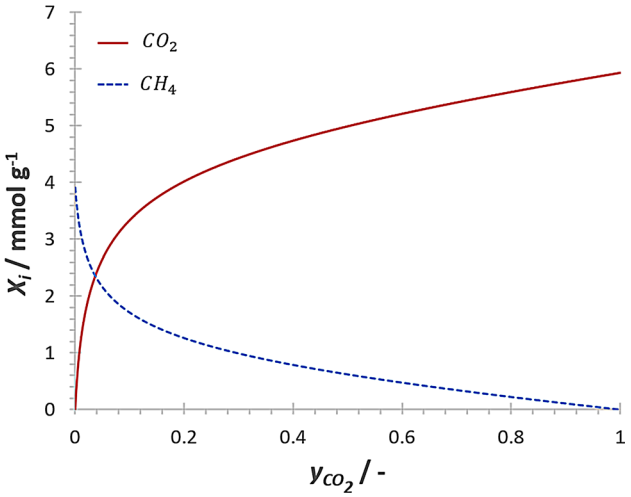

Fig. 15 Binary adsorption equilibria of CO_2 (red) and CH_4 (blue) on Ni-MOF-74 at $T = 303.15$ K and $p = 5$ bar

$$\frac{1}{n_t} = \sum_{i=1}^{n} \frac{x_i}{n_i\left(p_i^0\right)} + \sum_{i=1}^{n} x_i \left(\frac{\partial ln\gamma_i}{\partial z}\right)_{T,\vec{x}} \tag{19}$$

with

$$n_i = x_i n_t \tag{20}$$

Equation (16), (17) and (19) can be simplified by setting the activity coefficient to one under requirement of the adsorbate–adsorbate interactions being by orders of magnitude smaller compared to the adsorbate-adsorbent interactions, which can be assumed to be satisfied for the given system.

Based on the pure component's adsorption equilibria (see Fig. 7) the adsorption equilibrium of the binary mixture of CO_2 and CH_4 is being predicted by IAST as given in Fig. 15. With regard to the feed composition of the dynamic breakthrough experiment, with a molar fraction of CO_2 of 0.25, the binary equilibrium loadings are predicted to 4.24 mmol CO_2 per g and 1.11 mmol CH_4 per g, respectively.

By comparison of the dynamic adsorption uptake and the equilibrium uptakes (see Table 2) a boost in CO_2 capacity by the factor of 1.58–2.42 can be observed which can be attributed to the storage function of the employed mesoporous Al_2O_3 core. With regard to the adsorption selectivity an even higher impact by the factor of 55.02 can be found. This phenomenon can be attributed to the different uptake kinetics which are clearly favoring CO_2. The selectivity was calculated as to White and Lassettre [24]:

$$\alpha_{CO_2(,CH_4)} = \frac{X_{CO_2} y_{CH_4}}{y_{CO_2} X_{CH_4}} \tag{21}$$

Hence the core shell composite appears to be far from thermodynamic equilibrium with regard to the dynamic experiments since the BTC and RTD are not overlapping at the end of the breakthrough experiments (see Fig. 10), which is indicated by the fact that the concentrations at the adsorber outlet still deviate from the feed composition. This means that at the beginning of the experiment the adsorbent is being saturated with the faster diffusing CO_2 until the concentration at the adsorber outlet approximates the feeds concentration and the slower diffusing CH_4 starts to replace the CO_2. These observations have been verified by replication experiments.

4 Conclusions

A new core–shell species was introduced by hydrothermal synthesis of Ni-MOF-74 on spherical Al_2O_3 carrier substrates. By means of optical and scanning electron microscopy as well as methods of material characterization (volumetric adsorption with N_2/CO_2 and fluid displacement experiments with He) it was proven that a continuous Ni-MOF-74 layer was deposited onto the Al_2O_3 core with a mass fraction of 3.0–4.6. Kinetic experiments with Ni-MOF-74@Al_2O_3 core–shell composites—measured at 303.15 K and various pressures—exposed remarkably dominating uptake rates for CO_2 over CH_4 even though the latter appears to be in favor with regard to the equilibrium loadings at higher pressures. By comparing the adsorption uptake derived from dynamic breakthrough experiments (at 303.15 K and 500 kPa) to corresponding adsorption equilibria with Ni-MOF-74 it was shown, that the capacity and selectivity towards the key component

Table 2 Comparison of the equilibrium adsorption uptake and selectivity of Ni-MOF-74 for pure CO_2 (X_{eq}) and for the binary mixture calculated by IAST ($X_{IAST}, \alpha_{CO_2,IAST}$) to those of Ni-MOF-74@$Al_2O_3$ derived from dynamic breakthrough experiments ($X_{dyn}, \alpha_{CO_2,dyn}$) at reference conditions: $T = 303.15$ K, $p = 5$ bar and $y_{CO_2} = 0.25$

Adsorptive	X_{eq} (mmol g^{-1})	X_{IAST} (mmol g^{-1})	X_{dyn} (mmol g^{-1})	$\alpha_{CO_2,IAST}$ (−)	$\alpha_{CO_2,dyn}$ (−)
CO_2	4.41	4.24	6.85–10.51	11.46	630.6
CH_4	2.82	1.11	0.03–0.05	–	–

CO_2 was increased by the factor of 1.58–2.42 and 55.02, respectively. Thus, the application of core–shell composites occurs to be a promising approach in terms of adsorptive CO_2 separation due to a kinetic-induced boost in separation efficiency.

In summary Ni-MOF-74@Al_2O_3 core shell composites unite several different benefits of an attractive adsorbent for the separation of CO_2 from CH_4. The use of mesoporous core material coated with the selective MOF material allows to produce adsorbents with diameters applicable in an industrial scale and overcomes the problem of compounding and sintering in order to avoid large pressure drops. In addition, the thin core enables vast material savings, whereas the selectivity and uptake capacity can be increased simultaneously to a certain extent. Future research will rely on more detailed kinetic studies, pressure dependency and hysteresis behavior of this novel adsorbent in further dynamic adsorption experiments.

Funding Open access funding provided by Projekt DEAL.

Compliance with ethical standards

Conflict of interest All authors declare that they have no conflict of interest.

References

1. Hirscher M (2010) Handbook of hydrogen storage: new materials for future energy storage. Wiley, Weinheim
2. Whiston MM, Azevedo IL, Litster S, Whitefoot KS, Samaras C, Whitacre JF (2019) Expert assessments of the cost and expected future performance of proton exchange membrane fuel cells for vehicles. Proc Natl Acad Sci USA 116:4899–4904
3. Ryckebosch E, Drouillon M, Vervaeren H (2011) Techniques for transformation of biogas to biomethane. Biomass Bioenerg 35:1633–1645
4. Sørensen B (2017) Renewable energy: physics, engineering, environmental impacts, economics and planning. Academic Press, London
5. Starr K, Gabarrell X, Villalba G, Talens L, Lombardi L (2012) Life cycle assessment of biogas upgrading technologies. Waste Manag 32:991–999
6. Zhang X, Chen A, Zhong M, Zhang Z, Zhang X, Zhou Z, Bu X-H (2019) Metal–organic frameworks (MOFs) and MOF-derived materials for energy storage and conversion. Electrochem Energ Rev 2:29–104
7. Ramos-Fernandez EV, Garcia-Domingos M, Juan-Alcañiz J, Gascon J, Kapteijn F (2011) MOFs meet monoliths: hierarchical structuring metal organic framework catalysts. Appl Catal A 391:261–267
8. Han S, Wei Y, Valente C, Lagzi I, Gassensmith JJ, Coskun A, Stoddart JF, Grzybowski BA (2010) Chromatography in a single metal–organic framework (MOF) crystal. J Am Chem Soc 132:16358–16361
9. Peralta D, Chaplais G, Paillaud J-L, Simon-Masseron A, Barthelet K, Pirngruber GD (2013) The separation of xylene isomers by ZIF-8: a demonstration of the extraordinary flexibility of the ZIF-8 framework. Microporous Mesoporous Mater 173:1–5
10. MacGillivray LR, Lukehart CM (2014) Metal–organic framework materials. EIC books. Wiley, Hoboken
11. Zhu Q-L, Xu Q (2014) Metal–organic framework composites. Chem Soc Rev 43:5468–5512
12. Mahzoon S, Fatemi S, Hashemi SJ (2012) Modeling based investigation of ultrafine SAPO-34 core–shell adsorbent in cyclic adsorption process for purification of natural gas from CO_2. IJTAN 1:90–98
13. Sorribas S, Zornoza B, Serra-Crespo P, Gascon J, Kapteijn F, Téllez C, Coronas J (2016) Synthesis and gas adsorption properties of mesoporous silica-NH 2 -MIL-53(Al) core–shell spheres. Microporous Mesoporous Mater 225:116–121
14. Sorribas S, Zornoza B, Téllez C, Coronas J (2012) Ordered mesoporous silica-(ZIF-8) core–shell spheres. Chem Commun 48:9388–9390
15. Dasgupta S, Divekar S, Aarti, Spjelkavik AI, Didriksen T, Nanoti A, Blom R (2015) Adsorption properties and performance of CPO-27-Ni/alginate spheres during multicycle pressure-vacuum-swing adsorption (PVSA) CO_2 capture in the presence of moisture. Chem Eng Sci 137:525–531
16. Dietzel PDC, Besikiotis V, Blom R (2009) Application of metal–organic frameworks with coordinatively unsaturated metal sites in storage and separation of methane and carbon dioxide. J Mater Chem 19:7362
17. Kwapinski W, Salem K, Mewes D, Tsotsas E (2010) Thermal and flow effects during adsorption in conventional, diluted and annular packed beds. Chem Eng Sci 65:4250–4260
18. Sips R (1948) On the structure of a catalyst surface. J Chem Phys 16:490–495
19. Sips R (1950) On the structure of a catalyst surface. II. J Chem Phys 18:1024–1026
20. Burden RL, Faires JD (2001) Numerical analysis, 7th edn. Brooks/Cole, Pacific Grove
21. Myers AL, Prausnitz JM (1965) Thermodynamics of mixed-gas adsorption. AIChE J 11:121–127
22. Walton KS, Sholl DS (2015) Predicting multicomponent adsorption: 50 years of the ideal adsorbed solution theory. AIChE J 61:2757–2762
23. Talu O, Zwiebel I (1986) Multicomponent adsorption equilibria of nonideal mixtures. AIChE J 32:1263–1276
24. White D, Lassettre EN (1960) Theory of ortho-para hydrogen separation by adsorption at low temperatures, isotope separation. J Chem Phys 32:72–84